Available online at www.sciencedirect.com

ScienceDirect

Procedia CIRP 137 (2025) 374–379

www.elsevier.com/locate/procedia

CIRP Conference on Electro Physical and Chemical Engineering

Laser powder bed fusion of 3D metamaterials for energy absorption

Wessel W. Wits[a,b,*], Camill de Vos[a], Maria Montero-Sistiaga[a] and Marc de Smit[a]

[a]*Metal Additive Manufacturing Technology Centre (MAMTeC), NLR – Royal Netherlands Aerospace Centre, Marknesse, the Netherlands*
[b]*Faculty of Electrical Engineering, Mathematics and Computer Science, University of Twente, Enschede, the Netherlands*

* Corresponding author. *E-mail address:* w.w.wits@utwente.nl

Abstract

Metamaterials with unique energy absorption properties are fabricated by additive manufacturing. Manufacturing limitations, imposed by Laser Powder Bed Fusion (LPBF), hamper the production of in particular 3D metamaterial structures, due to unsupported overhanging struts that are part of the unit cell design. This study analyses two types of 3D metamaterials, the auxetic re-entrant and octet truss. Optimal process parameters are determined experimentally for stainless steel 316L and unit cell design parameters are related to the overall performance of the metamaterial lattices. Drop-weight impact testing experiments are conducted on LPBF-fabricated metamaterial samples. Unique properties for energy absorption, directly related to the metamaterial's unit cell design, are demonstrated.

Keywords: Metamaterials; Additive manufacturing; Laser powder bed fusion; Auxetic re-entrant lattice; Octet truss lattice; Impact testing; Energy absorption

1. Introduction

Metamaterials are engineered lattice structures with unique properties not found in nature, such as negative refractive index, perfect absorption, negative thermal conductivity or negative Poisson's ratio [1]. In the case of a periodic lattice, these properties arise from the complex, repeating structure (i.e. the unit cell) that can be designed to exhibit specific characteristic metamaterial behaviour. Recently, Additive Manufacturing (AM) technologies have revolutionised, amongst others, the field of metamaterials by enabling the efficient and economic production of complex lattice structures [2-3]. AM technologies offer local tailorability, freeform capability, tool-free fabrication and flexibility in geometric coverage allowing for the design and fabrication of complex structures, such as metamaterials, with predefined mechanical properties. This has opened up new avenues for research in various fields, including aerospace, defence, energy, biomedical and others [4].

Mechanical metamaterials feature counterintuitive mechanical properties arising from their unit cell architecture [5]. Recent studies have examined AM-fabricated mechanical metamaterials, including those with high-energy absorption and large deformability [6-7]. For energy absorption, the focus of this study, Stanczak et al. [8] studied the energy absorption properties of various lattice designs fabricated by Laser Powder Bed Fusion (LPBF) by exposing them to a blast compression test. They conclude that a 3D unit cell can absorb more energy compared to a 2D-extruded type of unit cell. However, manufacturing limitations, such as those imposed by LPBF, make it challenging to produce certain part features [9]. In particular, parts that include overhanging structures, such as 3D metamaterial lattices, are difficult to manufacture. To improve the manufacturability of metamaterial structures, researchers have adapted the design of the unit cell e.g. by replacing overhanging struts with inclined struts or by incorporating support material into the unit cell [10-11]. These approaches are however suboptimal, as they compromise the desired metamaterial behaviour by changing the design of the unit cell.

From a manufacturing point of view, the selection of LPBF process parameters specifically for the fabrication of 3D lattice structures featuring many individual struts that come together at the nodal positions is challenging. Karami et al. [12]

2212-8271
10.1016/j.procir.2025.02.278

considered both continuous and pulsed laser power to improve the properties of Ti6Al4V lattice structures. The former resulting in fewer imperfections, while the latter results in a more homogenous microstructure. Vrána et al. [13] demonstrated the fabrication of 35° AlSi10Mg struts by applying a 25% scan track overlapping strategy. Di Prima et al. [14] reported that laser offset adjustments produce noticeable changes in the strut diameter of Ti6Al4V lattices. More practically, Groβmann et al. [15] proposed a scaling law that relates the width of a single melt track to the laser power and scan speed for processing low-density lattice structures. Their model however assumes that melt pool consolidation is done on top of an already solidified track allowing for good heat conduction from the melt pool to the build plate, while for overhanging struts of 3D metamaterials this is clearly not the case. Accordingly, Beevers et al. [16] concluded that optimal process parameters for lattice structures differ significantly from bulk material parameters.

The goal of this study is to optimise LPBF process conditions specifically for 3D metamaterials featuring a unit cell design with horizontal struts build without a solid structure underneath. The performance of fabricated 3D metamaterials will be assessed based on energy absorption by drop-weight impact testing.

2. Experimental design and data analysis

For this study, two types of unit cell design are selected to investigate the manufacturability by LPBF and associated energy absorption behaviour. First, the 3D auxetic re-entrant lattice is selected, see Fig. 1(a), as this type of lattice structure exhibits a negative Poisson's ratio. Hence, the structure will contract laterally when compacted longitudinally. This unusual behaviour is achieved through the specific arrangement of the unit cell, which is characterized by inward-pointing members that connect to the lattice nodes. The advantages of auxetic re-entrant lattices include their potential for improved energy absorption and a unique deformation behaviour. Second, the 3D octet truss lattice is selected, see Fig. 1(b), as this type is mechanically more suitable to support loads in multiple directions. The octet truss lattice is known for its high strength-to-weight ratio, making it a popular choice for applications where lightweight yet robust structures are required, such as in aerospace engineering or architecture. The advantages of an octet truss lattice include its high stiffness, resistance to buckling and ability to withstand various types of loading. For both 3D re-entrant and 3D octet truss lattices, manufacturing limitations and cost currently hamper large-scale application.

a) 3D auxetic re-entrant b) 3D octet truss

Fig. 1. Studied types of metamaterial lattice designs (three adjacent unit cells placed on support pillars for LPBF fabrication are depicted).

LPBF fabrication of both metamaterial lattice structures is not straightforward, due to the large number of horizontal struts that are part of the unit cell design. The aim here is to enable direct LPBF fabrication of the afore unit cell designs rather than modifying the designs to accommodate manufacturing limitations thereby compromising metamaterial behaviour. Hence, the LPBF process parameters need to be matched with the sizing of the unit cell and constituent members. This is done in a first experiment, in which a full-factorial experimental design is performed. The unit cell size and the strut diameter are varied between 4 mm and 8 mm, and 0.3 mm and 0.7 mm, respectively, for both the 3D re-entrant and 3D octet truss unit cell designs. The resulting structures are examined visually to select optimal parameter combinations for the second experiment, in which a number of complete 3D metamaterial lattices is fabricated for functional energy absorption testing.

The metamaterial lattices are fabricated on a Nikon SLM Solution 280HL machine using Stainless Steel 316L (SS316L) as powder feedstock material. SS316L is selected because of its high elongation at break property (up to 60%), which is ideal for large deformations of the unit cell. Also, Smith et al. [17] examined yield stress and energy absorption characteristics of SS316L lattices and concluded that good impact protection is achievable due to the uniform collapse response of lattices.

LPBF process parameters are derived from an earlier test campaign that focused on consolidating scan tracks on powder rather than on a previously solidified structure. Contour line scanning is performed with a laser power and scan speed of 150 W and 450 mm/s, respectively, while downskin parameters are set to 125 W and 400 mm/s, respectively. In this case, resulting single track widths are in the order of 150-200 µm. Hence, the smallest 0.3 mm strut diameter consists of just two adjacent contour line scans.

After fabrication, a stress-relief heat treatment at 1095 °C for 4h and successive rapid cooling from 900 °C to room temperature under an argon environment is applied. Finally, the metamaterial lattices are removed from the build plate by wire Electrical Discharge Machining (EDM).

Functional testing of the metamaterial lattices is performed by drop-weight impact testing. An impactor of 5.658 kg is dropped onto the metamaterial lattices from a height of 4.5 m resulting in a nominal impact energy of 250 J. The impactor is equipped with a load cell that measures the impact force during the impact at 250 kHz. Just before impacting, the velocity of the impactor, which is used to compute the actual impact energy, is determined by an optical sensor. This sensor also triggers a high-speed camera that is used to observe the impact. A Photron Fastcam SA5 is used to capture the impact and lattice deformation with a frame rate of 7200 fps and an image resolution of 1024 x 752 pixels per frame.

During the impact, the metamaterial lattices drastically deform as energy is absorbed by the structure. The equivalent stress, σ_{eq}, during the time of impact is determined by:

$$\sigma_{eq}(t) = \frac{F(t)}{A_{eff}} \quad (1)$$

where, $F(t)$ is the force-time series acquired from the impactor load cell and A_{eff} is the effective surface area of the

metamaterial lattice perpendicular to the impact direction. The surface area of the lattice is measured before the impact test.

The force-time series are reformulated as a deceleration-time series by scaling with the mass of the impactor. By time integration and using the measured initial velocity at impact by the optical sensor, the time evolution of the velocity decrease is determined. In a second time-integration step, the depth of impact, *x(t)*, is determined. By scaling with the measured original height of the metamaterial lattice, h_0, the equivalent strain during the time of impact is determined according to:

$$\varepsilon_{eq}(t) = \frac{x(t)}{h_0} \tag{2}$$

To evaluate the characteristic behaviour and performance of the metamaterial lattices to absorb the impact energy, the stress-strain plot for each type of lattice is examined. Typically, three characteristic regimes can be observed in the stress-strain plot of a lattice structure during compressive deformation [7]. For a stretch-dominated lattice, a generalised stress-strain plot is illustrated in Fig. 2. First, a linear-elastic regime is present up to the initial yielding point. Second, a stress plateau is reached characterised by a constant average stress-strain curve although sequential local collapsing of unit cells within the lattice is observable. Third, a densification regime is present, in which the stress rapidly increases indicating that unit cells are internally colliding causing direct material-to-material contacts, subsequently loosing characteristic metamaterial behaviour.

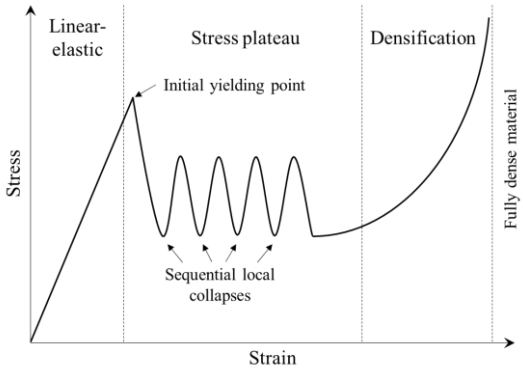

Fig. 2. Generalised stress-strain plot for a stretch-dominated lattice under compression deformation; redrawn from [7].

To determine the onset of densification, the energy absorption efficiency during the time of impact is determined according to:

$$\eta(\varepsilon) = \frac{1}{\sigma_{eq}(\varepsilon)} \int_0^{\varepsilon} \sigma_{eq}(\varepsilon_{eq}) d\varepsilon \tag{3}$$

Here, a peak in absorption efficiency is defined as the end point of the stress plateau regime and starting point for the densification regime, following the approach of Li et al. [18].

In conjunction, the total energy that is absorbed by the metamaterial lattice is also evaluated. Hereto, the Specific Energy Absorption (SEA) is determined, as the work done per unit mass of the metamaterial lattice, according to:

$$SEA = \frac{\int_0^{\varepsilon} \sigma_{eq}(\varepsilon_{eq}) d\varepsilon}{m} \tag{4}$$

where, *m* is the measured mass of the metamaterial lattice.

3. Results and discussion

A selection of the fabricated samples of the first experiment is shown in Fig. 3. The effect of an increasing strut diameter from 0.3 mm to 0.7 mm is depicted. The samples on the left-hand side of the images show that if the strut diameter is too thin, the build fails. In this case, the horizontal struts are not strong enough and detach from one end of the connection points. After consolidation before recoating, they bend upwards due to thermal stresses. If this process repeats for a number of layers, the struts will protrude through a newly deposited powder layer and hit the recoater during recoating, resulting in the breakage patterns visible in Fig. 3.

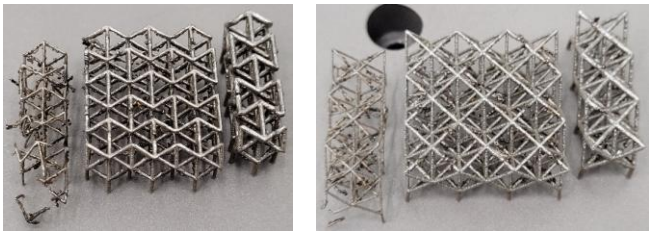

a) 3D auxetic re-entrant b) 3D octet truss

Fig. 3. Results of first experiment to find optimal LPBF process parameters and unit cell dimensions for the 3D metamaterial lattices.

Similar to a too small strut diameter, also if the unit cell size is selected too large, the build fails. The experiment showed that a strut diameter of 0.3 mm was too thin in all cases, and for a strut diameter of 0.5 mm only the smallest 4 mm unit cell size gives successful results. This led to the selection of eight combinations of unit cell design parameters for the fabrication of metamaterial lattices of approximately 32 x 32 x 25 mm^3, as listed in Table 1, for the second experiment. The exact dimensions vary a little due to the sizing of the unit cell itself. From the nominal mass, it can be observed that the unit cell density of the octet truss is about 40% higher than the unit cell density of the auxetic re-entrant.

Table 1. Experimental design of metamaterials' unit cell and nominal mass of the complete lattice (appr. 32 x 32 x 25 mm^3) for the second experiment.

Unit cell type - Sample ID	Unit cell size [mm]	Strut diameter [mm]	Nominal mass [g]
Re-entrant - 8 – Ø0.7	8	Ø0.7	14.3
Re-entrant - 6 – Ø0.7	6	Ø0.7	21.6
Re-entrant - 4 – Ø0.7	4	Ø0.7	44.9
Re-entrant - 4 – Ø0.5	4	Ø0.5	24.2
Octet truss - 8 – Ø0.7	8	Ø0.7	19.8
Octet truss - 6 – Ø0.7	6	Ø0.7	28.7
Octet truss - 4 – Ø0.7	4	Ø0.7	63.8
Octet truss - 4 – Ø0.5	4	Ø0.5	35.4

Fig. 4 depicts the fabricated metamaterial lattices on the build plate. In the top left-hand corner four 3D auxetic re-entrant lattices are visible, while in the bottom right-hand corner four 3D octet truss structures are visible. The insets show a close-up of the lattices with a unit cell size of 6 mm.

To compare both unit cell types, the results of the drop-weight impact test of the smallest unit cell size and smallest strut diameter are shown in Fig. 5. The black and red lines refer to the re-entrant and octet truss structures, respectively. The dotted lines indicate the time evolution of the deceleration of the impactor computed from the force sensor data. Following

the aforementioned time integration, both the velocity of the impactor and the depth of impact are computed and visualised by the dashed and solid lines, respectively. Finally, the depth of impact resolved from image analysis of the high-speed camera is depicted by the solid line with markers indicating the individual frames.

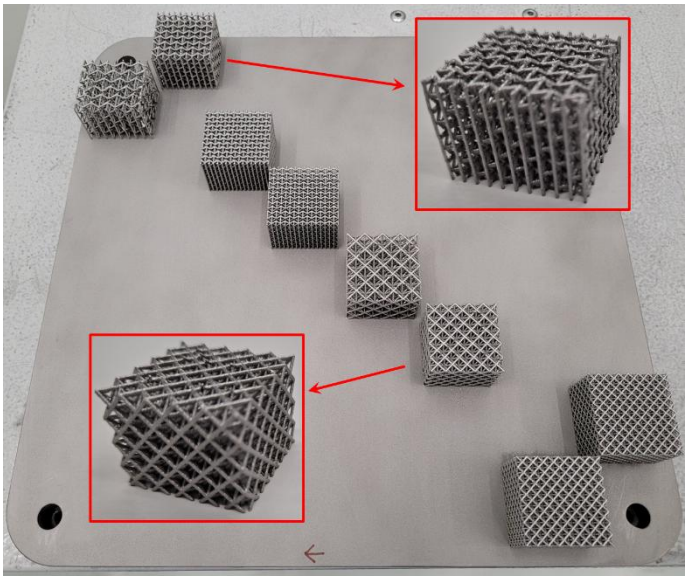

Fig. 4. Fabricated 3D metamaterial lattices by LPBF; insets show a close-up of the re-entrant and octet-truss lattices with a 6 mm unit cell size.

By comparing the time evolutions of the impactor deceleration, the octet truss lattice absorbs the energy such that the deceleration is maximised to a certain plateau similar to the generalised stretch-dominated lattice. As soon as all the impact energy is absorbed, the deceleration rapidly drops to zero. For the Octet truss - 4 – Ø0.5, this plateau is around 4 mm/s^2. This lattice is able to absorb the impact energy in about 2.7 ms. Conversely, for the auxetic re-entrant lattice, the impactor deceleration increases continuously at a lower rate and almost linearly with time to a maximum at which all the impact energy is absorbed. Compared to the octet truss lattice, deceleration is slower during the first 2 ms of the impact, resulting in a longer time duration of 3.3 ms to absorb an equal amount of impact energy. The progressive deceleration can be attributed to the auxetic behaviour of the unit cell. During the sequential local collapses material is drawn into the lattice structure, rather than being pushed out. Hence, the impactor sees progressively more material during the time evolution of the impact, resulting in a higher deceleration towards the end of the impact. This inward motion (i.e. negative Poisson's ratio) of the lattice is also visible in the top insets of Fig. 5.

The time evolution of the impactor velocity shows in both cases a negative velocity at the end of the impact. Also, on the high-speed camera video, some rebound effect of the impactor is observed. Moreover, as the integration constant is determined by the measured initial impact velocity, a time-integration error may accumulate. An offset is also observed by comparing the computed depth of impact with the observed images from the high-speed camera. The computed depth of impact is higher compared to the visually observed depth with an overshoot of 1.6 and 1.9 mm for the re-entrant and octet truss, respectively. Similar to the computed velocity error, here also a time-integration error may accumulate during the time of impact. Interestingly, for the lattice structures with a larger unit cell size, the computed and observed depths of impact match much better with an average deviation of 0.2 mm.

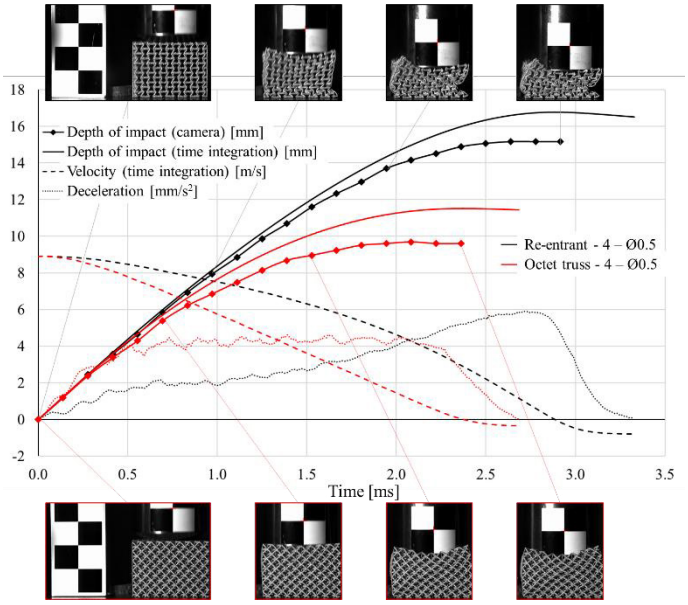

Fig. 5. Results of drop-weight impact testing of re-entrant and octet truss structures; insets are selected frames from high-speed camera imaging.

The inset high-speed camera images of Fig. 5 also highlight the behavioural difference between both types of unit cell design upon deformation. The auxetic re-entrant structure is deformed more due to local collapses of the unit cell and less material usage within the unit cell. Those collapses cause material to be drawn inwards progressively providing more material in the path of the collision. Conversely, while the unit cells of the octet truss also deform, they do not seem to totally collapse. In this case, the lattice bulges outwards pushing material away from the collision path. This characteristic behaviour related to the design of the unit cell is seen in all samples, as evidenced by Fig. 6. Henceforth, this is studied further by comparing the stress-strain responses.

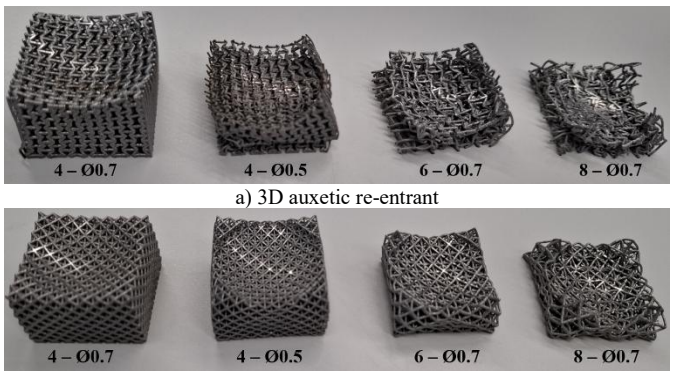

Fig. 6. Deformed 3D metamaterial lattice structures after impact testing ordered according to the resulting strain.

The equivalent stress-strain responses of all fabricated metamaterial lattices are depicted in Fig. 7. The responses of

the auxetic re-entrant lattices are different compared to the responses of the octet truss structures. For the most open structures, indicated by the blue lines, between a strain of about 20% to 70% a constant average stress plateau showing sequential local collapses is clearly visible. The average stress levels at the plateau are 2.3 MPa and 7 MPa for the auxetic re-entrant and octet truss structures, respectively. After 70% strain, the densification regime starts. At the end of the densification regime, the force levels reach the impact sensor's saturation level of 35 kN, clipping the signal. In practice, this means that the impactor is 'seeing' the assumed infinitely stiff table underneath the lattice and hence the lattice in between the impactor and the table is collapsed to a stiffness equivalent to the table. The most right images of Fig. 6 attest to this.

Conversely the densest structures, i.e. the smallest unit cell size and thickest strut diameter, indicated by the green lines, almost immediately exhibit a densification regime. The auxetic re-entrant structure shows a little over 20% strain including a number of local collapses, while the octet truss only reaches 10% strain without any local collapses. At this point, sensor saturation is reached indicating a densified material response equally stiff as the table, rather than metamaterial deformation.

For the other two intermittent types, indicated by the orange and red lines, the stress-strain curves also show a stress plateau starting at about 20% strain. For the auxetic re-entrant structures, the stress-strain curve curves up at about 50% strain, while continuously showing sequential local collapses. This strain-hardening effect can be attributed to the aforementioned negative Poisson's ratio of the re-entrant unit cell. Both octet trusses could absorb the total amount of impact energy, while for the auxetic Re-entrant - 6 – Ø0.7, indicate by the orange line, the force sensor went into saturation at 79% strain.

The effect of force sensor saturation can also be observed in Fig. 8. Here, the absorption efficiency, according to Equation (3), is plotted against the computed equivalent strain. Based on the computed position of the impactor, the absorbed energy is determined by time integration and compared to the initial impact energy determined from the initial velocity. This way the energy absorbance by metamaterial deformation is assessed. The insets of Fig. 8 list the percentage of the impact energy that was absorbed by metamaterial deformation.

The Fig. 8 inset shows that only the auxetic Re-entrant - 4 – Ø0.5 lattice is able to absorb the full impact energy. The three other re-entrant types either get fully densified or become too stiff before the total amount of impact energy could be absorbed by metamaterial deformation. For the Octet truss - 6 – Ø0.7 and Octet truss - 4 – Ø0.5, both lattices are able to absorb the full impact energy.

As expected, before reaching the densification regime both metamaterial types behave differently. Due to the auxetic behaviour of the re-entrant type, the absorption efficiency reaches a maximum efficiency of about 30% at about 50% strain. For the remaining strain, the maximum efficiency stays approximately at this plateau. Conversely, for the octet truss lattices the absorption efficiency increases linearly with the strain until a maximum efficiency at about 50% is reached. At that point, Octet truss - 8 – Ø0.7, the most open structure, is saturated and the densification regime starts, while for Octet truss - 6 – Ø0.7 and Octet truss - 4 – Ø0.5 all impact energy is already absorbed and the densification regime is not reached.

The results of Fig. 8 demonstrate that metamaterial behaviour is inherent to the unit cell design and not the unit size cell nor its strut diameter. Hence, depending on the application needs, the designer should select a unit cell design based on the required metamaterial behaviour. Subsequently, by tuning the unit cell size and strut diameter, the amount of energy absorption and strain can be matched with the foreseen impact loading conditions.

Table 2. Measured mass and Specific Energy Absorption (SEA).

Unit cell type - Sample ID	Measured mass [g]	Mass deviation [%]	SEA [kJ/kg]
Re-entrant - 8 – Ø0.7	14.4	+0.9	7.12
Re-entrant - 6 – Ø0.7	21.7	+0.4	9.01
Re-entrant - 4 – Ø0.7	45.9	+2.2	2.06
Re-entrant - 4 – Ø0.5	27.9	+15.6	8.00
Octet truss - 8 – Ø0.7	21.4	+8.0	7.66
Octet truss - 6 – Ø0.7	31.1	+8.4	7.20
Octet truss - 4 – Ø0.7	68.6	+7.5	0.46
Octet truss - 4 – Ø0.5	42.3	+19.5	5.28

Next to energy absorption efficiency, for applications in which mass is a critical design parameter, as it is for aerospace applications, the SEA is another important metamaterial attribute. Table 2 lists the measured mass and SEA, according to Equation (4), of each sample. Also, the deviation compared to the nominal mass is listed. All fabricated samples are heavier compared to the nominal mass, which is typical for LPBF due to adhesion of loose powder particles to the structures. Results show that for the smallest 0.5 mm strut diameter, the mass

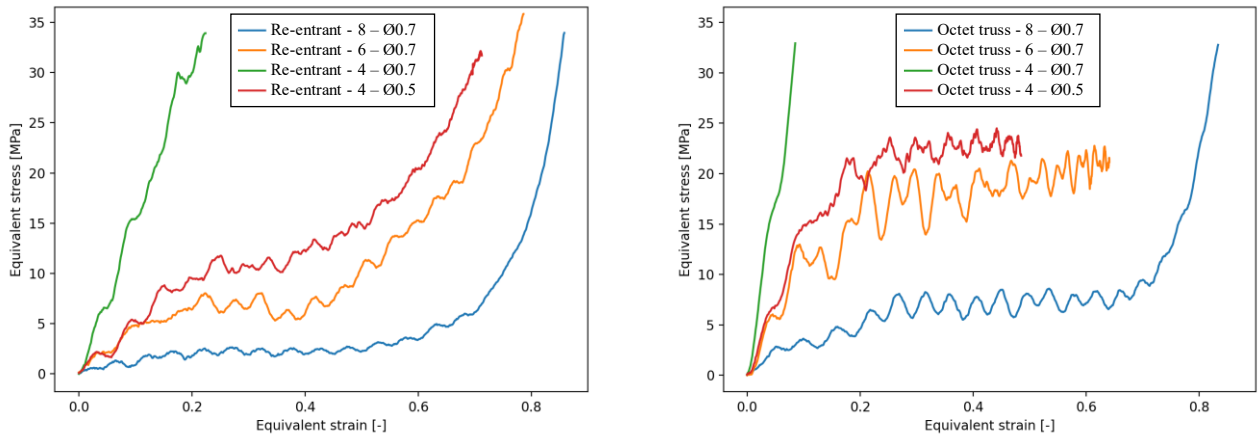

Fig. 7. Equivalent stress-strain responses of drop-weight impact testing using 5.658 kg from 4.5 m (i.e. 250 J).

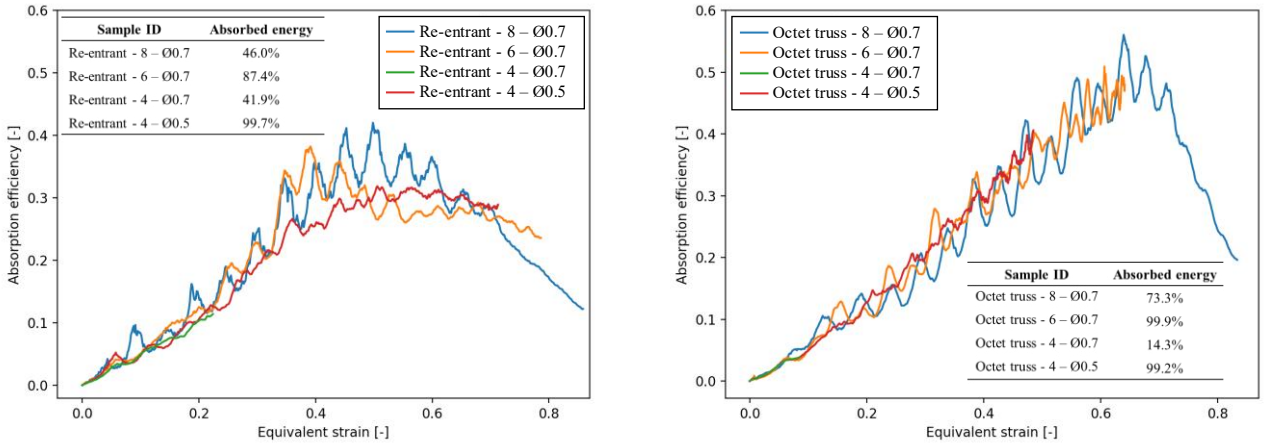

Fig. 8. Absorption efficiency of both metamaterial structures; inset lists the percentage of impact energy absorbed.

overshoot is most pronounced. Similarly, the octet truss structures show a higher overshoot compared to the re-entrant structures, which can be attributed to the fact that the unit cell of the octet truss contains more struts, and thus more volume, that needs to be consolidated during the LPBF process. Although the energy absorption efficiency is generally higher for the octet truss lattices, the specific energy absorption is generally higher for the auxetic re-entrant type. Hence, where mass is a crucial design parameter, the auxetic re-entrant type unit cell seems favourable.

4. Conclusions

Successful AM of 3D metamaterials for energy absorption has been demonstrated. LPBF process parameters are matched with unit cell sizes and strut diameters for unit cell designs of both auxetic re-entrant and octet truss types. Following a two-step experimental approach to select optimal combinations, eight 3D metamaterial lattices were successfully fabricated. Drop-weight impact testing was applied to characterise and assess the metamaterial performances.

Results demonstrate that LPBF is a suitable manufacturing technique for the fabrication of 3D metamaterials. Moreover, from the analysed impact energy responses, a two-step design approach can be formulated. First, the designer should match the design of the unit cell with application needs in terms of impact behaviour (i.e. maximise deceleration force or slower deceleration rate). Second, the design parameters of the unit cell itself should be matched with the expected energy absorption level and strain allowance of the application.

References

[1] J. E. Holliman, H. T. Schaef, B. P. McGrail, and Q. R. S. Miller, ‘Review of foundational concepts and emerging directions in metamaterial research: design, phenomena, and applications’, *Mater. Adv.*, vol. 3, no. 23, pp. 8390–8406, Nov. 2022, doi: 10.1039/D2MA00497F.

[2] M. Askari *et al.*, ‘Additive manufacturing of metamaterials: A review’, *Additive Manufacturing*, vol. 36, p. 101562, Dec. 2020, doi: 10.1016/j.addma.2020.101562.

[3] J. Fan *et al.*, ‘A review of additive manufacturing of metamaterials and developing trends’, *Materials Today*, vol. 50, pp. 303–328, Nov. 2021, doi: 10.1016/j.mattod.2021.04.019.

[4] M. Kadic, G. W. Milton, M. van Hecke, and M. Wegener, ‘3D metamaterials’, *Nat Rev Phys*, vol. 1, no. 3, pp. 198–210, Mar. 2019, doi: 10.1038/s42254-018-0018-y.

[5] X. Wu, Y. Su, and J. Shi, ‘Perspective of additive manufacturing for metamaterials development’, *Smart Mater. Struct.*, vol. 28, no. 9, p. 093001, Aug. 2019, doi: 10.1088/1361-665X/ab2eb6.

[6] P. Zhang, P. Yu, R. Zhang, X. Chen, and H. Tan, ‘Grid octet truss lattice materials for energy absorption’, *International Journal of Mechanical Sciences*, vol. 259, p. 108616, Dec. 2023, doi: 10.1016/j.ijmecsci.2023.108616.

[7] Y. Li, D. Jiang, R. Zhao, X. Wang, L. Wang, and L.-C. Zhang, ‘High Mechanical Performance of Lattice Structures Fabricated by Additive Manufacturing’, *Metals*, vol. 14, no. 10, Art. no. 10, Oct. 2024, doi: 10.3390/met14101165.

[8] M. Stanczak, T. Fras, L. Blanc, P. Pawlowski, and A. Rusinek, ‘Numerical and experimental study on mechanical behaviour of the AlSi10Mg aluminium structures manufactured additively and subjected to a blast wave’, *EPJ Web Conf.*, vol. 250, p. 02017, 2021, doi: 10.1051/epjconf/202125002017.

[9] M. K. Thompson *et al.*, ‘Design for Additive Manufacturing: Trends, opportunities, considerations, and constraints’, *CIRP Annals*, vol. 65, no. 2, pp. 737–760, Jan. 2016, doi: 10.1016/j.cirp.2016.05.004.

[10] J. Xiong, D. Gu, H. Chen, D. Dai, and Q. Shi, ‘Structural optimization of re-entrant negative Poisson’s ratio structure fabricated by selective laser melting’, *Materials & Design*, vol. 120, pp. 307–316, Apr. 2017, doi: 10.1016/j.matdes.2017.02.022.

[11] S. Li, H. Hassanin, M. M. Attallah, N. J. E. Adkins, and K. Essa, ‘The development of TiNi-based negative Poisson’s ratio structure using selective laser melting’, *Acta Materialia*, vol. 105, pp. 75–83, Feb. 2016, doi: 10.1016/j.actamat.2015.12.017.

[12] K. Karami *et al.*, ‘Continuous and pulsed selective laser melting of Ti6Al4V lattice structures: Effect of post-processing on microstructural anisotropy and fatigue behaviour’, *Additive Manufacturing*, vol. 36, p. 101433, Dec. 2020, doi: 10.1016/j.addma.2020.101433.

[13] R. Vrána *et al.*, ‘Selective Laser Melting Strategy for Fabrication of Thin Struts Usable in Lattice Structures’, *Materials*, vol. 11, no. 9, Art. no. 9, Sep. 2018, doi: 10.3390/ma11091763.

[14] M. Di Prima *et al.*, ‘Build parameter influence on strut thickness and mechanical performance in additively manufactured titanium lattice structures’, *Journal of the Mechanical Behavior of Biomedical Materials*, vol. 151, p. 106369, Mar. 2024, doi: 10.1016/j.jmbbm.2024.106369.

[15] A. Großmann, J. Felger, T. Frölich, J. Gosmann, and C. Mittelstedt, ‘Melt pool controlled laser powder bed fusion for customised low-density lattice structures’, *Materials & Design*, vol. 181, p. 108054, Nov. 2019, doi: 10.1016/j.matdes.2019.108054.

[16] E. Beevers, A. Cutolo, and B. Van Hooreweder, ‘Finetuning design and process conditions to minimise manufacturing deviations in strut-based metal lattice structures produced by Laser Powder Bed Fusion’, *Applied Materials Today*, vol. 42, p. 102551, Feb. 2025, doi: 10.1016/j.apmt.2024.102551.

[17] M. Smith *et al.*, ‘The quasi-static and blast response of steel lattice structures’, *Jnl of Sandwich Structures & Materials*, vol. 13, no. 4, pp. 479–501, Jul. 2011, doi: 10.1177/1099636210388983.

[18] Q. M. Li, I. Magkiriadis, and J. J. Harrigan, ‘Compressive Strain at the Onset of Densification of Cellular Solids’, *Journal of Cellular Plastics*, vol. 42, no. 5, pp. 371–392, Sep. 2006, doi: 10.1177/0021955X06063519.